Deuteron microscopic optical model potential

Hairui Guo (郭海瑞),[1,*] Yongli Xu (徐永丽),[1,2] Yinlu Han (韩银录),[1,†] and Qingbiao Shen (申庆彪)[1]

[1]*China Institute of Atomic Energy, Post Office Box 275(41), Beijing 102413, People's Republic of China*

[2]*College of Physics and Electronic Science, Shanxi Datong University, Datong 037009, People's Republic of China*

(Received 21 December 2009; revised manuscript received 10 February 2010; published 28 April 2010)

A deuteron microscopic optical model potential is obtained by the Green function method through nuclear-matter approximation and local-density approximation based on the effective Skyrme interaction. The microscopic optical model potential is used to calculate the deuteron reaction cross sections and the elastic scattering angular distributions for some target nuclei in the mass range $6 \leqslant A \leqslant 208$ with incident deuteron energies up to 200 MeV. The calculated results are compared with the experimental data.

DOI: 10.1103/PhysRevC.81.044617 PACS number(s): 24.10.Ht, 25.45.−z, 24.10.Cn

I. INTRODUCTION

The optical model is one of the most important theoretical models in nuclear reaction theory, which makes a strong impact on many branches of nuclear reaction physics. The phenomenological optical model potential is obtained by adjusting its parameters to minimize the deviation between the calculated results and the existing experimental values of reaction cross sections and elastic scattering angular distributions, which can often reproduce the experimental data quite well, but cannot predict the scattering without experimental data with certainty. The microscopic optical model potential (MOP) is generated theoretically based on the nucleon-nucleon interaction, which has significant application for the scattering without experimental data, especially for the scattering from unstable nuclei in nuclear astrophysics.

The reaction induced by deuteron is of great interest in many fields, such as radiation damage estimation, radioactive waste transmutation, and so on. Therefore, the research on deuteron optical model potential is of great value. At present, there are many deuteron phenomenological optical model potentials [1–4], some of which are global phenomenological optical model potentials [2–4]. The global phenomenological optical model potential from Daehnick *et al.* [2] is based on two sets of reaction cross sections and some elastic scattering angular distributions, the global potential from Bojowald *et al.* [3] is based on only some elastic scattering angular distributions, and the global potential from Han *et al.* [4] is based on more extensive reaction cross sections and elastic scattering angular distributions. There also exist some deuteron optical potentials constructed from folding model [5–8]. The deuteron optical potentials from Watanabe [5] and Perey and Satchler [6] are obtained by folding the phenomenological optical potentials for neutrons and protons, and the deuteron optical potential from Avrigeanu *et al.* [7,8] consists of a real folding potential and a phenomenological imaginary potential. Schuck [9] derived a deuteron optical potential, but the concrete expression for a deuteron optical potential was not given. The purpose of this paper is to present a different approach to obtaining the microscopic optical model potential for deuteron and give the concrete optical model potential.

An isospin-dependent nucleon microscopic optical potential [10,11] is obtained using the Green function method. In this method, as the nucleon optical model potential can be identified with the mass operator of the one-particle Green function from the view of the many-body theory [12], the mass operator is utilized to get the microscopic optical potential based on the Skyrme interaction through nuclear-matter approximation and local-density approximation. The theoretical results calculated by the nucleon microscopic optical potential are in good agreement with the experimental data. This method is also used to derive the microscopic optical potential for helium-3 [13], and the theoretical results are in reasonable agreement with the experimental data. Encouraged by these, the Green function method is utilized in the present paper to obtain the microscopic optical potential for deuteron. Using this method, the microscopic optical potential for deuteron is obtained from the two-particle Green function based on the Skyrme interaction, and the nuclear-matter approximation and local-density approximation are also used. The first-order mass operator of the two-particle Green function denotes the real part of the deuteron optical model potential, and the imaginary part of second-order mass operator denotes the imaginary part of the potential. The microscopic optical model potential obtained is used to calculate the reaction cross sections and the elastic scattering angular distributions in the mass range $6 \leqslant A \leqslant 208$ with incident deuteron energies up to 200 MeV, and the results are compared with experimental data.

In Sec. II, the formulation of the MOP for deuteron is presented. The calculated results and analysis are given in Sec. III. Finally, in Sec. IV a summary is given.

II. THEORETICAL MODEL

The Hamiltonian of the system composed of an incident particle and a target nucleus, which refers only to the two-body interaction, can be expressed as

$$H = H_0 + H_1, \tag{1}$$

*ghr@ciae.ac.cn
†hanyl@ciae.ac.cn

where

$$H_0 = \sum_i (t_i + U_i), \tag{2}$$

$$H_1 = \frac{1}{2}\sum_{i\neq j} V_{ij} - \sum_i U_i. \tag{3}$$

H_0 is the single-particle Hamiltonian, H_1 is the residual interaction, and U_i is the single-particle mean field.

The two-particle Green function is expressed as

$$\begin{aligned} &iG(\alpha_1\alpha_2, \beta_1\beta_2; t_1 - t_2) \\ &= \frac{\langle\phi_0|T\left[U_\eta(\infty, -\infty)\xi_{\alpha_2}(t_1)\xi_{\alpha_1}(t_1)\xi^+_{\beta_1}(t_2)\xi^+_{\beta_2}(t_2)\right]|\phi_0\rangle}{\langle\phi_0|U_\eta(-\infty, +\infty)|\phi_0\rangle} \\ &= \langle\phi_0|T\left[U_\eta(-\infty, +\infty)\xi_{\alpha_2}(t_1)\xi_{\alpha_1}(t_1)\xi^+_{\beta_1}(t_2)\xi^+_{\beta_2}(t_2)\right]|\phi_0\rangle_L, \end{aligned} \tag{4}$$

where $|\phi_0\rangle$ is the eigenstate of H_0, T is the time-ordering symbol, ξ_{α_1} and ξ_{α_2} are the particle annihilation operators in interaction representation, $\xi^+_{\beta_1}$ and $\xi^+_{\beta_2}$ are the particle creation operators in interaction representation, and L denotes that only the linked diagrams are reserved. $U_\eta(\infty, -\infty)$ is the time-evolution operator expressed as

$$\begin{aligned} U_\eta(\infty, -\infty) = \sum_{n=0}^{\infty}\left(\frac{-i}{\hbar}\right)^n \frac{1}{n!}\int d\tau_1 \int d\tau_2 \cdots\cdots \\ \times \int d\tau_n \exp[-\eta(|\tau_1| + |\tau_2| + \cdots\cdots + |\tau_n|)] \\ \times T\{H_1(\tau_1)H_1(\tau_2)\cdots\cdots H_1(\tau_n)\}, \end{aligned} \tag{5}$$

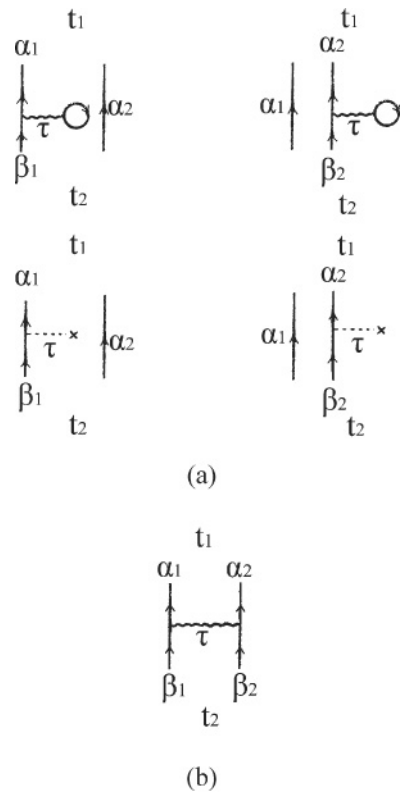

FIG. 1. First-order Feynman diagrams of the two-particle Green function.

where η is the infinitesimal introduced from adiabatic approximation.

The two-particle Green function satisfies the Dyson equation,

$$\begin{aligned} &iG(\alpha_1\alpha_2, \beta_1\beta_2; \omega) \\ &= iG^{(0)}(\alpha_1\alpha_2, \beta_1\beta_2; \omega) + \frac{i}{\hbar}\sum_{\rho\lambda\mu\nu} iG^{(0)}(\alpha_1\alpha_2, \rho\lambda; \omega) \\ &\quad \times [U_{\rho\lambda,\mu\nu} - M(\rho\lambda, \mu\nu; \omega)]iG(\mu\nu, \beta_1\beta_2; \omega), \end{aligned} \tag{6}$$

where $U_{\rho\lambda,\mu\nu}$ is the mean field and $M(\rho\lambda, \mu\nu; \omega)$ is the mass operator, which can be expanded into

$$M(\rho\lambda, \mu\nu; \omega) = M^{(1)}(\rho\lambda, \mu\nu; \omega) + M^{(2)}(\rho\lambda, \mu\nu; \omega) + \cdots. \tag{7}$$

For the scattering process, the mass operator $M(\alpha_1\alpha_2, \alpha_1\alpha_2; \omega)$ of the two-particle Green function is identified with the microscopic optical model potential for deuteron.

The two-particle Green function can be expanded into a perturbation series:

$$\begin{aligned} &iG(\alpha_1\alpha_2, \beta_1\beta_2; t_1 - t_2) \\ &= iG^{(0)}(\alpha_1\alpha_2, \beta_1\beta_2; t_1 - t_2) + iG^{(1)}(\alpha_1\alpha_2, \beta_1\beta_2; t_1 - t_2) \\ &\quad + iG^{(2)}(\alpha_1\alpha_2, \beta_1\beta_2; t_1 - t_2) + \cdots. \end{aligned} \tag{8}$$

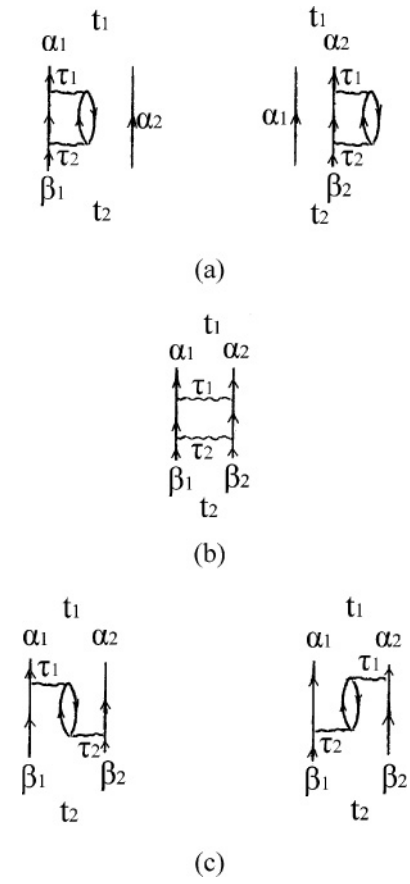

FIG. 2. The residual second-order diagrams of the two-particle Green function.

It is considered only approximately up to the second order in this article, and the corresponding Feynman diagrams include 1 zeroth-order diagram, 5 first-order diagrams given in Fig. 1, and 33 second-order diagrams.

As studying the deuteron optical potential, deuteron must be considered as a cluster and the nucleon-nucleon direct interaction in deuteron is not considered. Because the Feynman diagram in Fig. 1(b) describes the direct interaction of the two nucleons in deuteron, only the Feynman diagrams in Fig. 1(a) contribute to the first-order term of the two-particle Green function. By performing the Fourier transformation, the first-order term of the two-particle Green function can be expressed as

$$\begin{aligned} &iG^{(1)}(\alpha_1\alpha_2,\beta_1\beta_2;\omega) \\ &= \frac{i}{\hbar} iG^{(0)}_{\alpha_1\alpha_2}(\omega)\left[U_{\alpha_1\beta_1} - \sum_\rho V_{\alpha_1\rho,\beta_1\rho} n_\rho\right] iG^{(0)}_{\alpha_2\beta_1}(\omega)\delta_{\alpha_2\beta_2} \\ &\quad + \frac{i}{\hbar}\delta_{\alpha_1\beta_1} iG^{(0)}_{\alpha_1\alpha_2}(\omega)\left[U_{\alpha_2\beta_2} - \sum_\rho V_{\alpha_2\rho,\beta_2\rho} n_\rho\right] iG^{(0)}_{\alpha_1\beta_2}(\omega), \end{aligned} \tag{9}$$

where

$$n_\rho = \begin{cases} 1, & \text{below the Fermi surface,} \\ 0, & \text{above the Fermi surface,} \end{cases} \tag{10}$$

$$V_{\alpha\rho,\beta\rho} = \langle \alpha\rho | V | \beta\rho \rangle_A, \tag{11}$$

where A denotes antisymmetrization and V is the two-body nucleon-nucleon interaction.

From the Dyson equation, the first-order term of the two-particle Green function can also be expressed as

$$\begin{aligned} &iG^{(1)}(\alpha_1\alpha_2,\beta_1\beta_2;\omega) \\ &= \frac{i}{\hbar} iG^{(0)}_{\alpha_1\alpha_2}(\omega)[U_{\alpha_1\alpha_2,\beta_1\beta_2} - M^{(1)}(\alpha_1\alpha_2,\beta_1\beta_2;\omega)] iG^{(0)}_{\beta_1\beta_2}(\omega). \end{aligned} \tag{12}$$

Under the mean-field approximation,

$$U_{\alpha_1\alpha_2} = M^{(1)}_{\alpha_1\alpha_2}, \tag{13}$$

so $M^{(1)}_{\alpha_1\alpha_2}$ gives the real part of the MOP for deuteron. By comparing Eq. (9) and Eq. (12), the real part of the MOP for deuteron can be obtained:

$$M^{(1)}_{\alpha_1\alpha_2} = \sum_\rho V_{\alpha_1\rho,\alpha_1\rho} n_\rho + \sum_\rho V_{\alpha_2\rho,\alpha_2\rho} n_\rho. \tag{14}$$

In the right-hand side of Eq. (14), each term is just the contribution of the real part of the microscopic optical potential for each nucleon [10,11] in deuteron.

Under the mean-field approximation, 28 of the second-order Feynman diagrams are offset. The residual second-order Feynman diagrams are given in Fig. 2. The Feynman diagram in Fig. 2(b) describes the direct interaction between the two nucleons in deuteron, which can be ignored. The Feynman diagrams in Fig. 2(c) describe the indirect interactions between the two nucleons in deuteron, which can make deuteron break up. In this work, the Feynman diagrams in Fig. 2(c) are also ignored. Then only the Feynman diagrams in Fig. 2(a) contribute to the second-order term of the two-particle Green function.

By performing Fourier transformation, the second-order term of the two-particle Green function can be expressed as

$$\begin{aligned} &iG^{(2)}(\alpha_1\alpha_2,\beta_1\beta_2;\omega) \\ &= -\delta_{\alpha_1\beta_1} iG^{(0)}_{\alpha_1\alpha_2}(\omega)\frac{i}{\hbar}\left[\frac{1}{2}\sum_{\rho\delta\lambda}\frac{V_{\alpha_2\lambda,\delta\rho}V_{\delta\rho,\beta_2\lambda}}{\omega - \varepsilon_{\alpha_1} - \varepsilon_\rho - \varepsilon_\delta + \varepsilon_\lambda + i\eta} n_\lambda(1-n_\delta)(1-n_\rho)\right] iG^{(0)}_{\alpha_1\beta_2}(\omega) \\ &\quad - iG^{(0)}_{\alpha_1\alpha_2}(\omega)\frac{i}{\hbar}\left[\frac{1}{2}\sum_{\rho\delta\lambda}\frac{V_{\alpha_1\lambda,\delta\rho}V_{\delta\rho,\beta_1\lambda}}{\omega - \varepsilon_{\alpha_2} - \varepsilon_\rho - \varepsilon_\delta + \varepsilon_\lambda + i\eta} n_\lambda(1-n_\delta)(1-n_\rho)\right] iG^{(0)}_{\alpha_2\beta_1}(\omega)\delta_{\alpha_2\beta_2}, \end{aligned} \tag{15}$$

where

$$\omega = \varepsilon_{\alpha_1} + \varepsilon_{\alpha_2}. \tag{16}$$

Here the energy of each nucleon in deuteron is half the incident deuteron energy, namely,

$$\varepsilon_{\alpha_1} = \varepsilon_{\alpha_2} = \frac{\omega}{2}. \tag{17}$$

From the Dyson equation, the second-order term of the two-particle Green function can also be expressed as

$$\begin{aligned} &iG^{(2)}(\alpha_1\alpha_2,\beta_1\beta_2;\omega) \\ &= -\frac{i}{\hbar} iG^{(0)}_{\alpha_1\alpha_2}(\omega) M^{(2)}(\alpha_1\alpha_2,\beta_1\beta_2;\omega) iG^{(0)}_{\beta_1\beta_2}(\omega). \end{aligned} \tag{18}$$

The second-order mass operator of the two-particle Green function can be obtained by comparing Eq. (15) with Eq. (18),

$$\begin{aligned} &M^{(2)}_{\alpha_1\alpha_2}(E) \\ &= \frac{1}{2}\sum_{\rho\delta\lambda}\frac{V_{\alpha_1\lambda,\delta\rho}V_{\delta\rho,\alpha_1\lambda}}{\varepsilon_{\alpha_1} - \varepsilon_\rho - \varepsilon_\delta + \varepsilon_\lambda + i\eta} n_\lambda(1-n_\delta)(1-n_\rho) \\ &\quad + \frac{1}{2}\sum_{\rho\delta\lambda}\frac{V_{\alpha_2\lambda,\delta\rho}V_{\delta\rho,\alpha_2\lambda}}{\varepsilon_{\alpha_2} - \varepsilon_\rho - \varepsilon_\delta + \varepsilon_\lambda + i\eta} n_\lambda(1-n_\delta)(1-n_\rho) \\ &= M^{(2)}_{\alpha_1}\left(\frac{E}{2}\right) + M^{(2)}_{\alpha_2}\left(\frac{E}{2}\right). \end{aligned} \tag{19}$$

The imaginary part of the second-order mass operator $M^{(2)}_{\alpha_1\alpha_2}(E)$ is considered as the imaginary part of the microscopic optical potential for deuteron. According to the formula of the principal value integral,

$$\frac{1}{x+i\eta} = P\left(\frac{1}{x}\right) - i\pi\delta(x), \tag{20}$$

the imaginary part of the MOP for deuteron can be obtained as follows:

$$\begin{aligned} W &= \mathrm{Im}M^{(2)}_{\alpha_1\alpha_2}(E) = -\frac{\pi}{2}\sum_{\rho\delta\lambda} V_{\alpha_1\lambda,\delta\rho}V_{\delta\rho,\alpha_1\lambda}n_\lambda(1-n_\delta) \\ &\quad\times(1-n_\rho)\delta(\varepsilon_{\alpha_1}-\varepsilon_\rho-\varepsilon_\delta+\varepsilon_\lambda) - \frac{\pi}{2}\sum_{\rho\delta\lambda} V_{\alpha_2\lambda,\delta\rho} \\ &\quad\times V_{\delta\rho,\alpha_2\lambda}n_\lambda(1-n_\delta)(1-n_\rho)\delta(\varepsilon_{\alpha_2}-\varepsilon_\rho-\varepsilon_\delta+\varepsilon_\lambda) \\ &= \mathrm{Im}M^{(2)}_{\alpha_1}\left(\frac{E}{2}\right) + \mathrm{Im}M^{(2)}_{\alpha_2}\left(\frac{E}{2}\right), \end{aligned} \tag{21}$$

where $\mathrm{Im}M^{(2)}_{\alpha_1}(\frac{E}{2})$ and $\mathrm{Im}M^{(2)}_{\alpha_2}(\frac{E}{2})$ are the contributions of the imaginary parts of the MOP for the two nucleons [10,11] in deuteron, respectively.

An important conclusion is obtained from Eqs. (14) and (21) that, as the indirect interactions of the two nucleons in deuteron are ignored, the microscopic optical potential for deuteron is the sum of the microscopic optical potentials for its constituent nucleons.

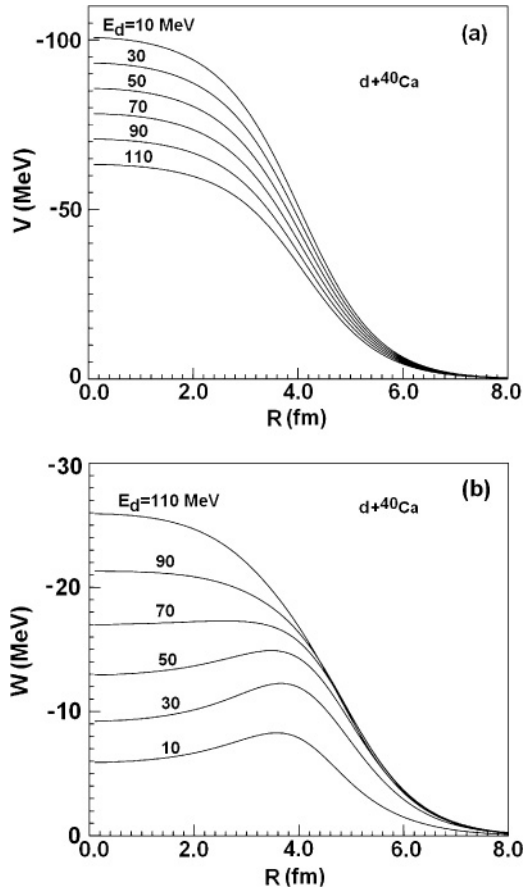

FIG. 3. Radial dependence of MOP for deuteron scattering from ^{40}Ca. (a) Real parts; (b) imaginary parts.

The interaction V in Eq. (11) is given by the extended Skyrme force GS2 as in Refs. [10,11,13], which can be expressed as

$$\begin{aligned} &V_{12}(\vec{R},\vec{r}) \\ &= t_0(1+x_0P_\sigma)\delta(\vec{r}) + \tfrac{1}{6}t_3(1+x_3P_\sigma)\rho^\alpha(\vec{R})\delta(\vec{r}) \\ &\quad + \tfrac{1}{2}t_1(1+x_1P_\sigma)[\vec{k}'^2\delta(\vec{r}) + \delta(\vec{r})\vec{k}^2] \\ &\quad + \tfrac{1}{2}t_4(1+x_4P_\sigma)[\vec{k}'^2\rho(\vec{R})\delta(\vec{r}) + \delta(\vec{r})\rho(\vec{R})\vec{k}^2] \\ &\quad + t_2(1+x_2P_\sigma)\vec{k}'\cdot\delta(\vec{r})\vec{k} + t_5(1+x_5P_\sigma)\vec{k}'\cdot\rho(\vec{R})\delta(\vec{r})\vec{k} \\ &\quad + iW_0(\vec{\sigma}_1+\vec{\sigma}_2)\cdot\vec{k}'\times\delta(\vec{r})\vec{k}. \end{aligned} \tag{22}$$

The parameters of GS2 are listed in Table I.

In nuclear matter, the wave function of nucleon α in Eq. (11) is given by the plane wave

$$\psi_\alpha(\vec{r}) = \frac{1}{\sqrt{\Omega}}e^{i\vec{k}_\alpha\cdot\vec{r}}\chi_{\sigma_\alpha}\chi_{\tau_\alpha}, \tag{23}$$

where χ_{σ_α} and χ_{τ_α} are the spin and isospin wave functions, respectively, and Ω is the volume.

When the distribution of the proton and neutron in deuteron is considered, the MOP for deuteron can be obtained by folding the microscopic optical potentials of its constituent nucleons in the ground state of deuteron. In the relative coordinate representation, the microscopic optical potential for deuteron can be expressed as

$$V_d(R) = \langle\phi_d|V_n\left(\vec{R}+\frac{\vec{r}}{2}\right) + V_p\left(\vec{R}-\frac{\vec{r}}{2}\right)|\phi_d\rangle, \tag{24}$$

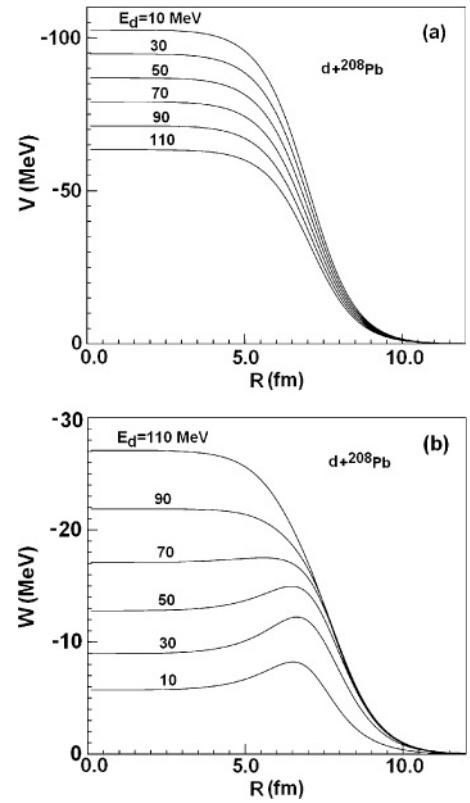

FIG. 4. Radial dependence of MOP for deuteron scattering from ^{208}Pb. (a) Real parts; (b) imaginary parts.

TABLE I. Extended Skyrme force GS2 parameters.

	t_0 (MeV fm^3)	t_1 (MeV fm^5)	t_2 (MeV fm^5)	t_3	t_4 (MeV fm^8)	t_5 (MeV fm^8)	α
GS2	−1177	670	−49.7	11 054	−775	0	1
	W_0 (MeV fm^5)	x_0	x_1	x_2	x_3	x_4	x_5
GS2	105	0.124	0	0	1	1	0

with $\vec{R}$ indicating the position of the center of mass of the deuteron and $\overrightarrow{r}$ indicating the position of the neutron in deuteron relative to the proton. V_n and V_p are the microscopic optical potentials for the neutron and the proton in deuteron, respectively, with half the incident deuteron energy. The expressions of V_n and V_p are taken as those in Refs. [10,11]. $\phi_d(r)$ is the ground-state wave function of deuteron, which can be expressed as a Hulthen function [12]:

$$\phi_d(r) = \frac{N_d}{r}[\exp(-\alpha r) - \exp(-\beta r)], \tag{25}$$

where $N_d = [\frac{\alpha\beta(\alpha+\beta)}{2\pi(\beta-\alpha)^2}]^{1/2}$, with $\alpha = 0.23$ fm and $\beta = 1.61$ fm.

Then the deuteron microscopic optical model potential can be expressed as

$$V_d(R) = 2\pi N_d^2 \iint [\exp(-\alpha r) - \exp(-\alpha r)]^2 (Vn + Vp) dr d\mu, \tag{26}$$

where $-1 \leqslant \mu \leqslant 1$.

The local-density approximation [14,15] is used to obtain the MOP for finite nuclei as in Refs. [10,11,13].

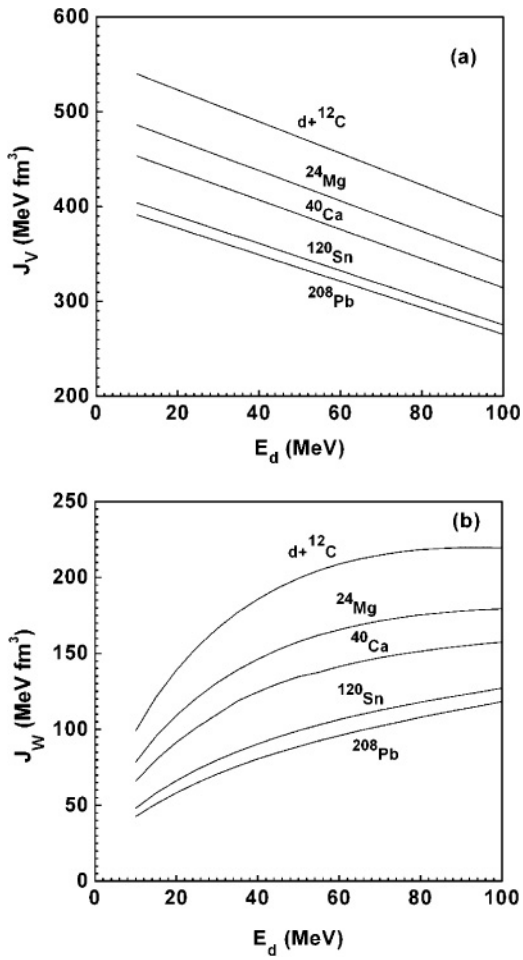

FIG. 5. The volume integral per nucleon of MOP for deuteron scattering from different nuclei against the incident energy E_d. (a) Real parts; (b) imaginary parts.

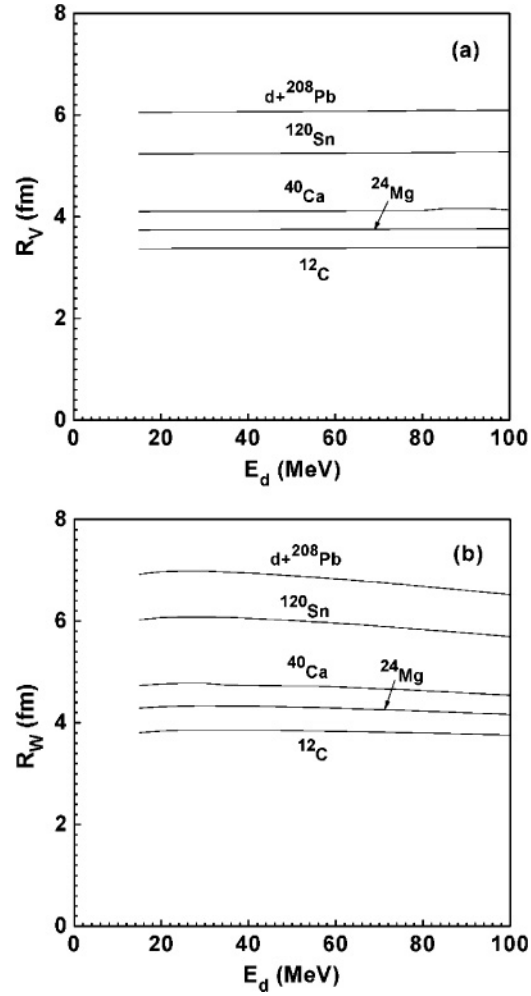

FIG. 6. The root-mean-square radii of MOP for deuteron scattering from different nuclei against incident energy. (a) Real parts; (b) imaginary parts.

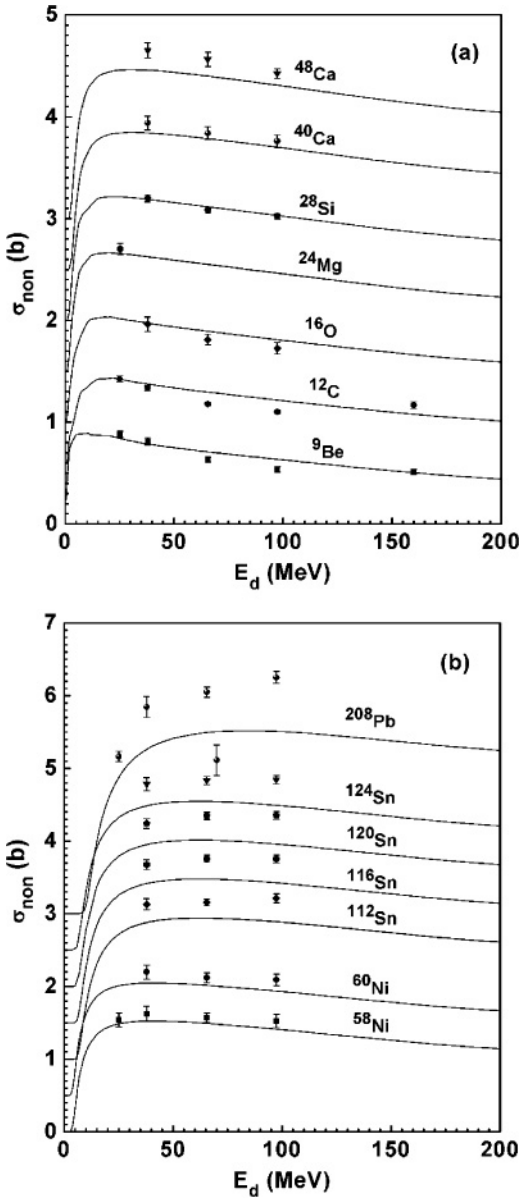

FIG. 7. Comparison between the calculated reaction cross sections (solid lines) for d + ^{9}Be, ^{12}C, ^{16}O, ^{24}Mg, ^{28}Si, ^{40,48}Ca, ^{58,60}Ni, ^{112,116,120,124}Sn, and ^{208}Pb reactions and experimental data (symbols)[19–22]. Different data sets are added by 0, 0.5, 1, 1.5, 2, 2.5, and 3, in turn.

The spin-orbit coupling potential for deuteron is considered as the sum of the spin-orbit potentials for its constituent nucleons. The energy-independent nucleon spin-orbit potential is obtained in Refs. [11,16]; however, in fact, the nucleon spin-orbit potential is energy dependent [17,18], which decreases with increasing energy. Therefore, an energy-dependent factor is introduced here:

$$V_{\rm SO}(r) = \frac{40}{E+40}\left(V_{\rm SO}^{n} + V_{\rm SO}^{p}\right). \tag{27}$$

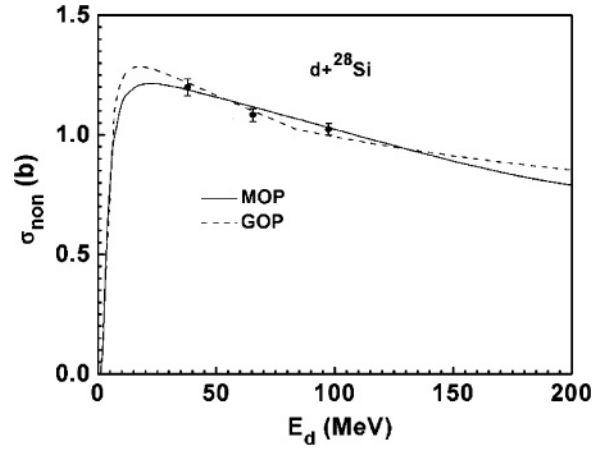

FIG. 8. Comparison between the calculated reaction cross section for d + ^{28}Si reaction and experimental data (symbols) [19]. The solid curve is calculated by the present MOP and the dashed curve is calculated by the global phenomenological optical potential (GOP) from Han *et al.* [4].

III. CALCULATED RESULTS AND ANALYSIS

The radial dependence, the volume integral per nucleon and the root mean square (rms) radii of the MOP for deuteron are calculated. The reaction cross sections and elastic scattering angular distributions are also predicted by the MOP for nuclides in the mass range $6 \leqslant A \leqslant 208$ with incident energies up to 200 MeV.

The radial dependence of the real and imaginary parts of the MOP for ^{40}Ca and ^{208}Pb at incident deuteron energies of

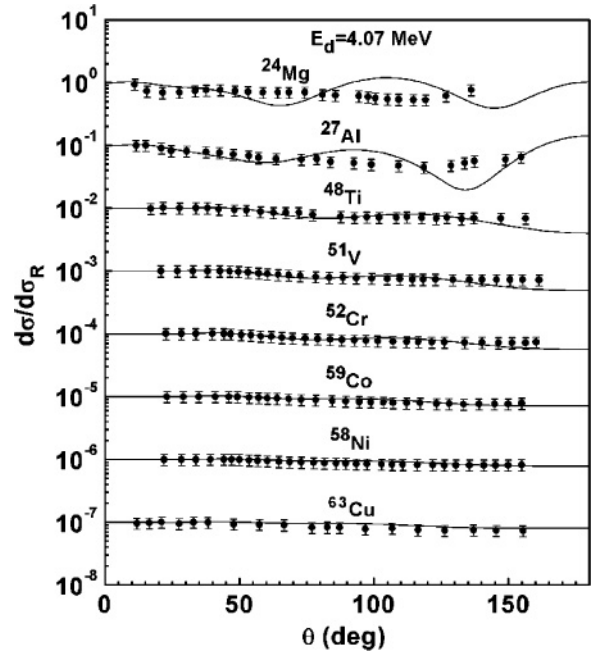

FIG. 9. Calculated elastic scattering angular distributions in the Rutherford ratio (solid line) at incident deuteron energy of 4.07 MeV compared with experimental data (symbols) [23]. The results are offset by a factor of 10.

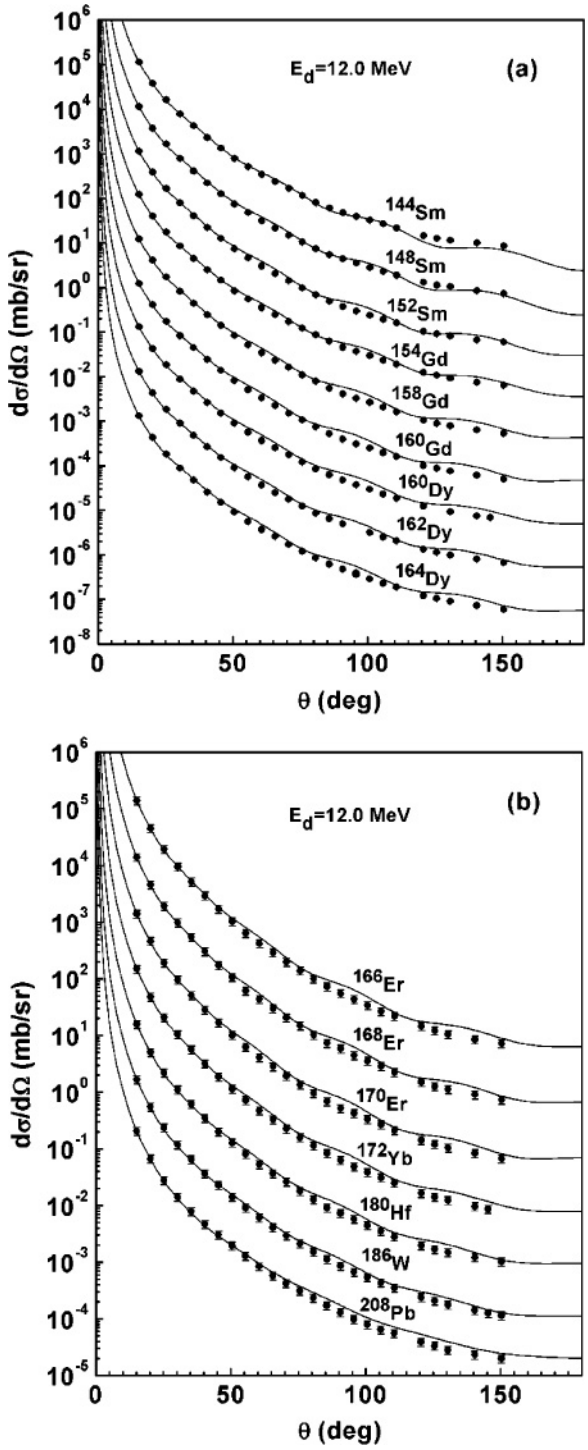

FIG. 10. Calculated elastic scattering angular distributions (solid lines) at an incident deuteron energy of 12.0 MeV compared with experimental data (symbols) [24]. The results are offset by factor of 10.

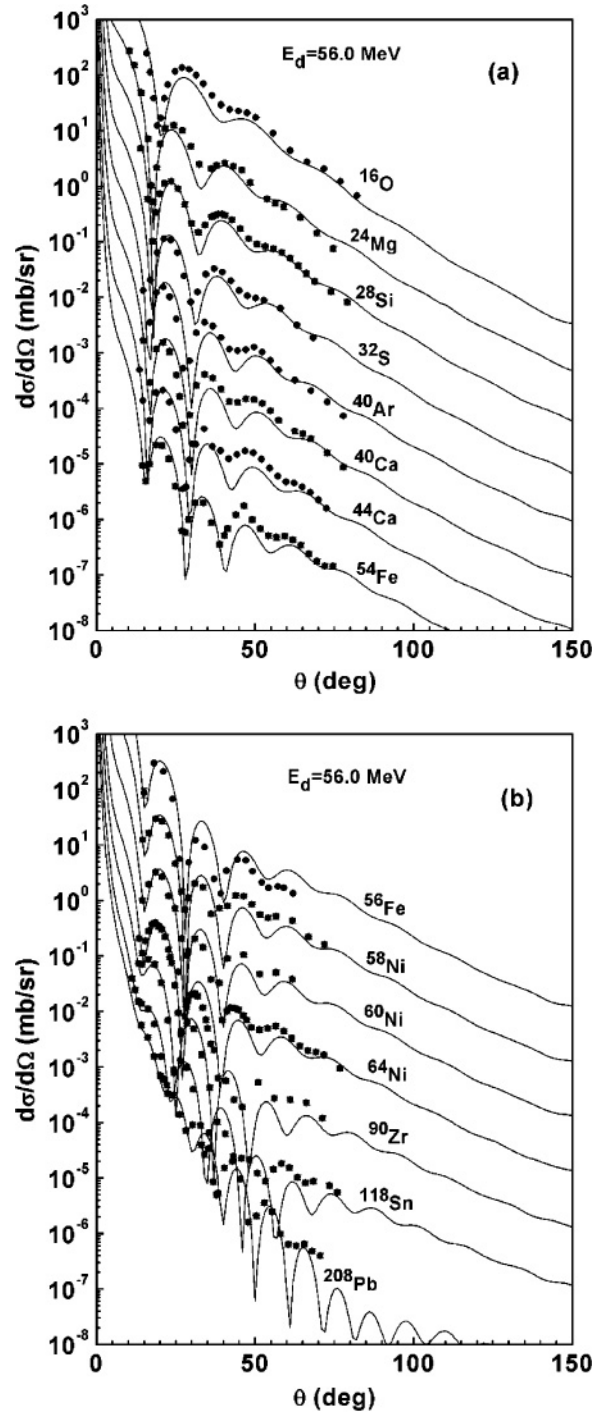

FIG. 11. Calculated elastic scattering angular distributions (solid lines) at an incident deuteron energy of 56.0 MeV compared with experimental data (symbols) [25]. The results are offset by a factor of 10.

10, 30, 50, 70, 90, and 110 MeV is shown in Figs. 3 and 4. In Fig. 3(a) and Fig. 4(a), the absolute value of the real part decreases with increasing radius and incident energy. In Fig. 3(b) and Fig. 4(b), the absolute value of the imaginary part increases with increasing energy of incident deuteron, and the primary contribution of the imaginary part changes from the surface absorption into the volume absorption as the incident energy increases. For the same incident energy, the contribution of the volume absorption of the imaginary part increases with increasing mass number of the target nucleus.

The volume integral per nucleon of the MOP for deuteron is expressed as

$$J_V = -\frac{1}{A_d A_T}\int V(r)d\vec{r}, \qquad J_W = -\frac{1}{A_d A_T}\int W(r)d\vec{r}, \tag{28}$$

and the rms radii is expressed as

$$\langle R_V^2\rangle^{1/2} = \left[\frac{\int V(r)r^2 d\vec{r}}{\int V(r)d\vec{r}}\right]^{1/2}, \qquad \langle R_W^2\rangle^{1/2} = \left[\frac{\int W(r)r^2 d\vec{r}}{\int W(r)d\vec{r}}\right]^{1/2}. \tag{29}$$

The energy dependence of them for ^{12}C, ^{24}Mg, ^{40}Ca, ^{120}Sn, and ^{208}Pb is shown in Figs. 5 and 6.

The volume integral per nucleon of the real and imaginary parts of the MOP decreases with increasing mass number as shown in Fig. 5. The volume integral per nucleon of the real part J_V is linearly dependent on the incident energy and decreases as the energy of the incident deuteron increases, while the volume integral per nucleon of the imaginary part J_W increases with increasing energy.

Figure 6 shows that the rms radii of the real and imaginary parts of the MOP increase with increasing mass number and keep basically as a constant.

The deuteron reaction cross sections for ^{9}Be, ^{12}C, ^{16}O, ^{24}Mg, ^{28}Si, ^{40,48}Ca, ^{58,60}Ni, ^{112,116,120,124}Sn, and ^{208}Pb are calculated with the MOP. The comparisons between calculated results and the experimental data [19–22] are given in Fig. 7. The figure shows that the calculated results for ^{16}O, ^{24}Mg, ^{28}Si, ^{40}Ca, and ^{58}Ni are in reasonable agreement with the experimental data. The shapes of the calculated results curves of reaction cross sections for ^{9}Be, ^{12}C, ^{48}Ca, ^{60}Ni, ^{112,116,120,124}Sn, and ^{208}Pb are similar to those of the experimental data, but the magnitudes of the calculated results

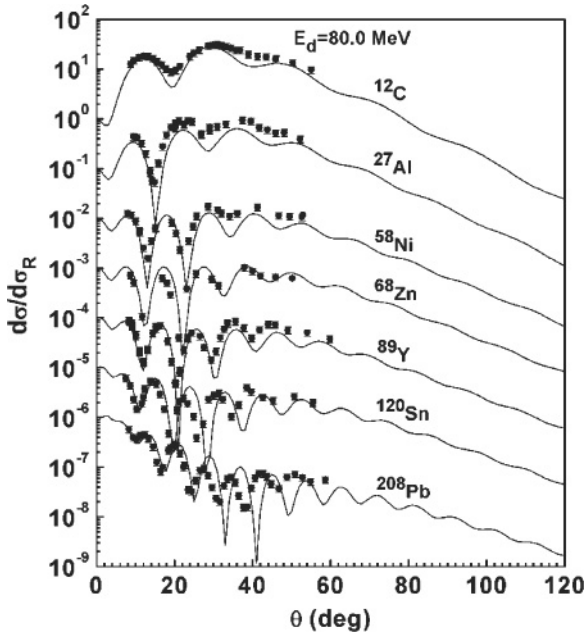

FIG. 12. Calculated elastic scattering angular distributions in the Rutherford ratio (solid lines) at an incident deuteron energy of 80.0 MeV compared with experimental data (symbols) [26–28]. The results are offset by a factor of 10.

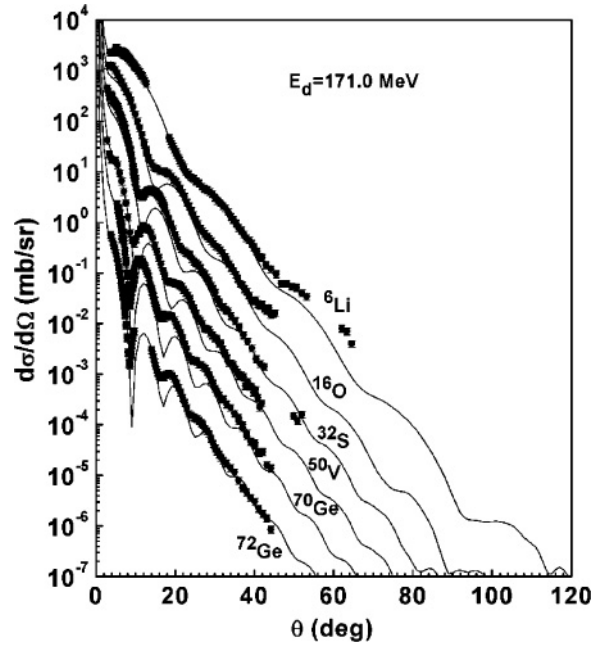

FIG. 13. Calculated elastic scattering angular distributions (solid lines) at an incident deuteron energy of 171.0 MeV compared with experimental data (symbols) [29]. The results are offset by a factor of 10.

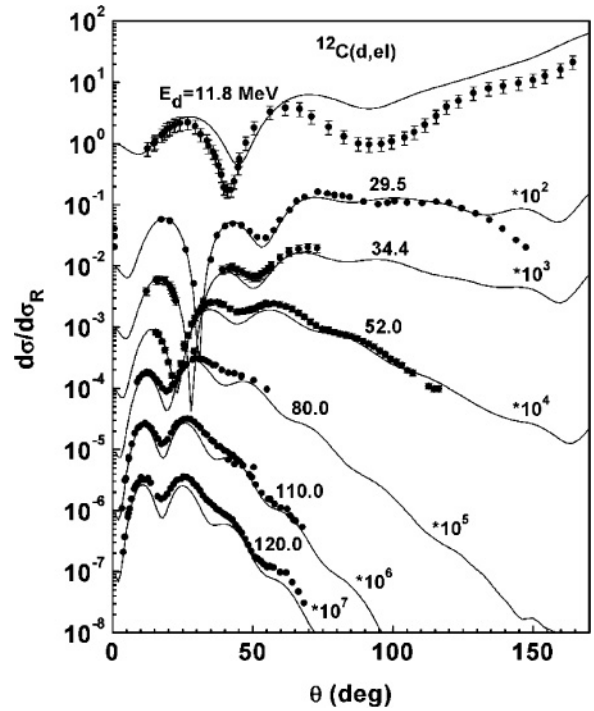

FIG. 14. Calculated elastic scattering angular distributions in the Rutherford ratio (solid lines) at different incident deuteron energies compared with experimental data (symbols) [30–35] for the $d + {}^{12}$C reaction.

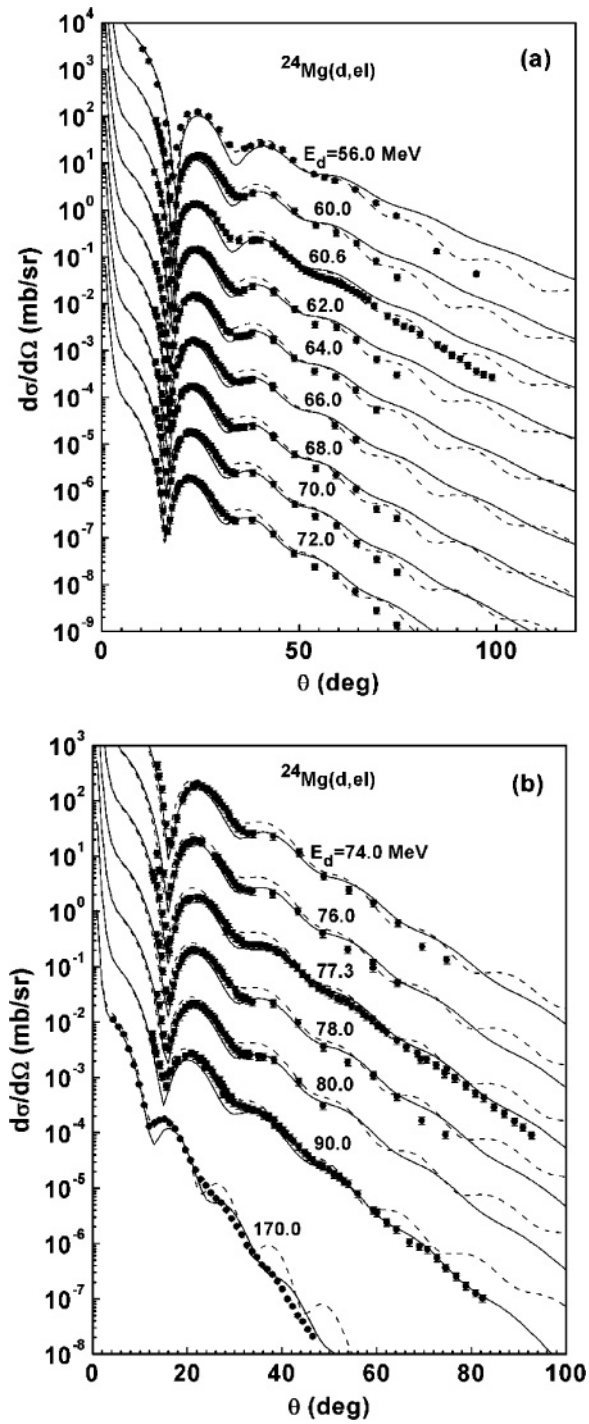

FIG. 15. Calculated elastic scattering angular distributions at different incident deuteron energies compared with experimental data (symbols) [36–38] for the $d + {}^{24}$Mg reaction. The solid curves are calculated by the present MOP and the dashed curves are calculated by the global phenomenological optical potential from Han *et al.* [4]. The results are offset by a factor of 10.

and the experimental data show some discrepancy. As deriving the MOP for deuteron in Sec. II, the indirect interactions of the two nucleons in deuteron is ignored; if this term is considered, the calculated reaction cross sections may be improved. Figure 7 also shows there is a general trend that the

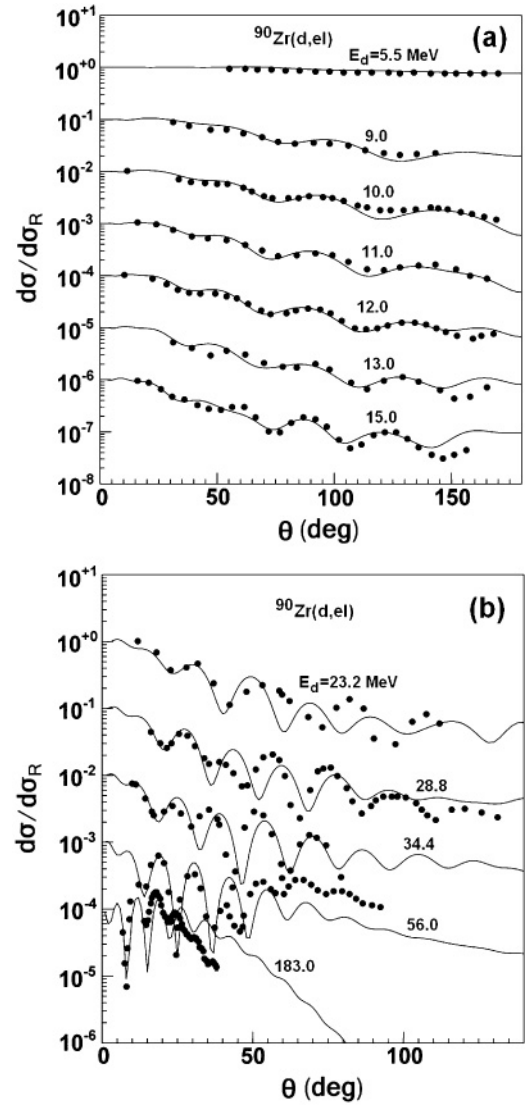

FIG. 16. Calculated elastic scattering angular distributions in the Rutherford ratio (solid lines) at different incident deuteron energies compared with experimental data (symbols) [32,36,39–46] for the $d + {}^{90}$Zr reaction. The results are offset by a factor of 10.

reaction cross sections increase with increasing mass number of the target nucleus.

The reaction cross sections for ^{12}C, ^{16}O, ^{28}Si, ^{40}Ca, and ^{58}Ni are calculated by the global deuteron optical potential from Han *et al.* [4] as well, and the results reproduce the experimental data very well. The present results calculated by MOP are comparable to those calculated by the global phenomenological potential in fitting the experimental data. Figure 8 gives an example with ^{28}Si.

The differential cross sections relative to Rutherford cross sections for elastic scattering of deuteron from ^{24}Mg, ^{27}Al, ^{48}Ti, ^{51}V, ^{52}Cr, ^{59}Co, ^{58}Ni, and ^{63}Cu at incident deuteron energy of 4.07 MeV are calculated, and the results are compared with the experimental data [23] in Fig. 9. The theoretical results for ^{24}Mg and ^{27}Al show some discrepancy with experimental data, while for other target nuclei the theoretical results are in good agreement with experimental data.

The comparisons of the calculated elastic scattering angular distributions for different target nuclei from ^{144}Sm to ^{208}Pb with experimental data [24] at incident deuteron energy of 12.0 MeV are given in Fig. 10. The theoretical results are in good agreement with experimental data.

The calculated results of the elastic scattering angular distributions for ^{16}O, ^{24}Mg, ^{28}Si, ^{32}S, ^{40}Ar, ^{40}Ca, ^{44}Ca, ^{54}Fe, ^{56}Fe, ^{58}Ni, ^{60}Ni, ^{64}Ni, ^{90}Zr, ^{118}Sn, and ^{208}Pb at incident deuteron energy of 56.0 MeV are compared with the experimental data [25] in Fig. 11. The theoretical values are in reasonable agreement with the experimental data.

The differential cross sections relative to Rutherford cross sections for elastic scattering of deuteron from ^{12}C, ^{27}Al, ^{58}Ni, ^{68}Zn, ^{89}Y, ^{120}Sn, and ^{208}Pb at incident energy of 80.0 MeV are calculated, and the results are compared with the experimental data [26–28] in Fig. 12. Reasonable agreement is obtained for all target nuclei.

The comparisons of the calculated elastic scattering angular distributions for ^{6}Li, ^{16}O, ^{32}S, ^{50}V, ^{70}Ge, and ^{72}Ge with experimental data [29] at incident deuteron energy of 171.0 MeV are given in Fig. 13. The theoretical results are in reasonable agreement with the experimental data.

The calculated results of differential cross sections relative to Rutherford cross sections for elastic scattering of deuteron from ^{12}C at incident energies from 11.8 to 120.0 MeV are compared with the experimental data [30–35] in Fig. 14. At incident energy of 11.8 MeV, the calculated results and the experimental data have some discrepancy, while at the incident energies from 29.5 to 120.0 MeV, the calculated results are in agreement with the experimental data.

The comparison between the calculated results of elastic scattering angular distributions and experimental data [36–38] for ^{24}Mg at incident deuteron energies from 56.0 to 170.0 MeV is given in Fig. 15. At the incident energies of 56.0, 60.0 and 60.6 MeV, a good agreement is obtained for angles below 70°, while for larger angles, the magnitudes of calculated results are larger than those of the experimental data. At the incident energies from 62.0 to 170.0 MeV, the calculated results are in good agreement with experimental data.

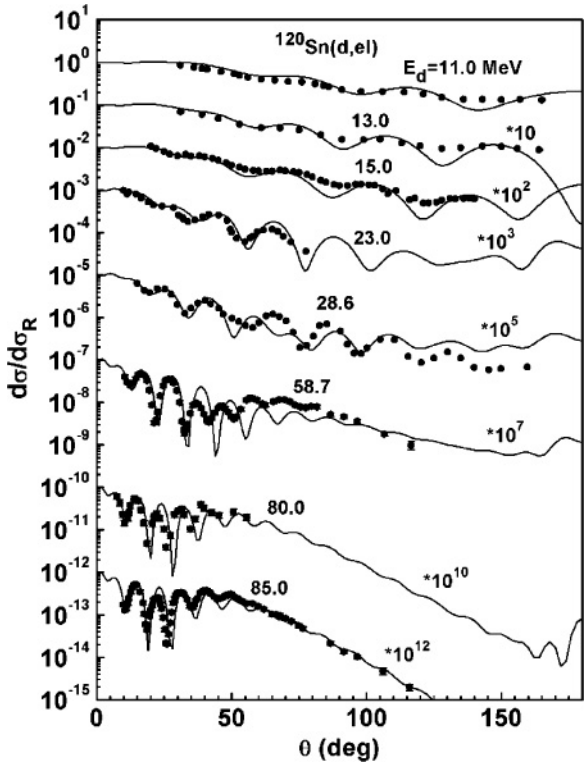

FIG. 17. Calculated elastic scattering angular distributions in the Rutherford ratio (solid lines) at different incident deuteron energies compared with experimental data (symbols) [3,34,40,44,47,48] for the $d + ^{120}$Sn reaction.

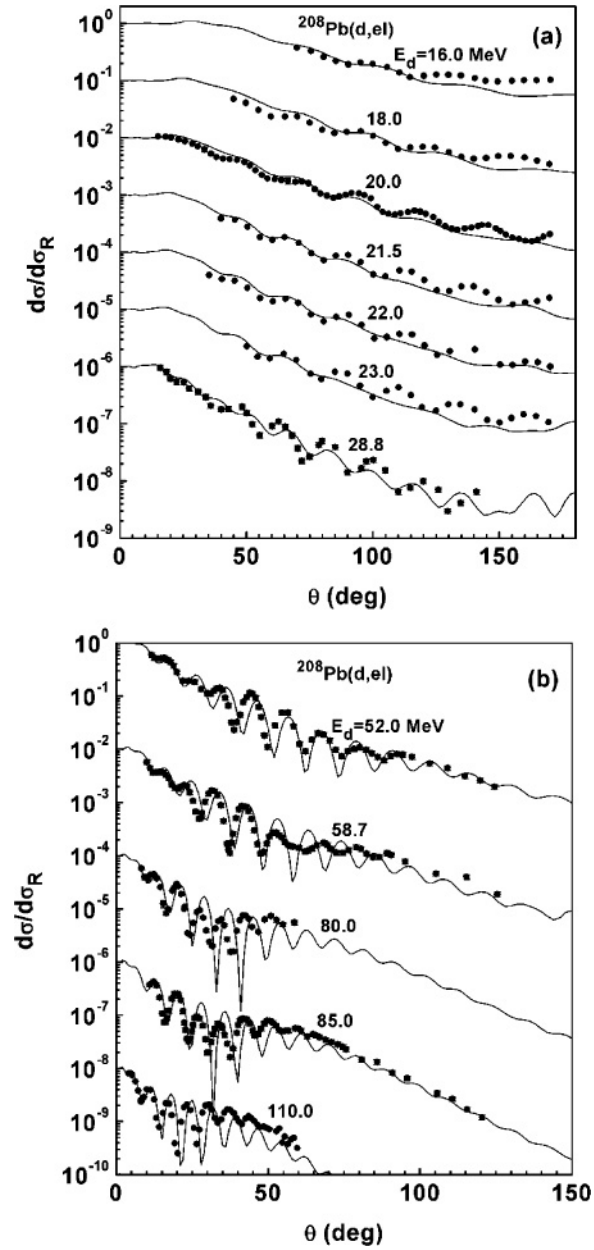

FIG. 18. Calculated elastic scattering angular distributions in the Rutherford ratio (solid lines) at different incident deuteron energies compared with experimental data (symbols) [3,33–35,44,45,49] for the $d + ^{208}$Pb reaction.

The calculated results of differential cross sections relative to Rutherford cross sections for elastic scattering of deuteron from ^{90}Zr at incident energies from 5.5 to 183.0 MeV are compared with the experimental data [32,36,39–46] in Fig. 16. The calculated results are in general agreement with experimental data.

The calculated results of differential cross sections relative to Rutherford cross sections for ^{120}Sn at incident deuteron energies from 11.0 to 85.0 MeV are compared with the experimental data [3,34,40,44,47,48] in Fig. 17. The calculated results are in reasonable agreement with experimental data.

The comparison between the calculated results of differential cross sections relative to Rutherford cross sections and experimental data [3,33–35,44,45,49] for ^{208}Pb at incident deuteron energies from 16.0 to 110.0 MeV is given in Fig. 18. The calculated results are in reasonable agreement with experimental data.

The differential cross sections relative to Rutherford cross sections for ^{12}C, ^{16}O, ^{27}Al, and ^{28}Si at incident deuteron energy of 52.0 MeV are calculated using the global phenomenological optical potential in Ref. [3], and the calculated results from the present microscopic optical model potential are better than that calculated by the global phenomenological optical potential in fitting the experimental data. The elastic scattering angular distributions for different nuclei at incident deuteron energies of 4.07, 12.0, and 171 MeV and for ^{24}Mg and ^{208}Pb at different incident deuteron energies are also calculated using the global phenomenological optical potential in Ref. [4]. Figure 15 gives the comparison between the elastic scattering angular distribution for ^{24}Mg calculated by the global potential and that calculated by the MOP, and it is shown that the calculated result from the present microscopic optical model potential is comparable to that calculated by the global phenomenological optical potential in fitting the experimental data. The calculated results for the other cases are similar to those for the case of ^{24}Mg.

The shape of the calculated results curve of elastic scattering angular distributions from our microscopic optical model potential is in good agreement with that of experimental data, but the magnitude has some discrepancy with that of experimental data for light target nuclei at lower incident deuteron energy. The reason for the discrepancy is that the light nuclei show a strong nuclear-structure effect at low incident energy and the mean-field approximation cannot describe the light nuclei well.

IV. SUMMARY

The deuteron microscopic optical model potential is obtained using a Green function method. The real part of the deuteron optical model potential is denoted by the first-order mass operator of the two-particle Green function, and the imaginary part potential is denoted by the imaginary part of second-order mass operator. The radial dependence, the volume integral per nucleon, and the rms radii of the MOP for deuteron are calculated, and the trend of the results is reasonable. Some reaction cross sections and elastic scattering angular distributions for target nuclides in the mass range $6 \leqslant A \leqslant 208$ with incident energies up to 200 MeV are also calculated by the deuteron microscopic optical model potential and compared with the experimental data. Except for the reaction cross sections for some target nuclei, the calculated results are generally in good agreement with the experimental data. Furthermore, some theoretical results calculated by the deuteron microscopic optical potential are comparable to ones calculated by deuteron global optical potential in fitting the experimental data.

Although our model calculation reproduces most experimental data well, but fails to reproduce the reaction cross sections for some target nuclei. This may suggest that the indirect interactions of the two nucleons in deuteron have an important effect on the MOP for deuteron. Therefore, the effect of the indirect interactions of the two nucleons in deuteron will be studied in the future.

ACKNOWLEDGMENTS

This work is one of National Basic Research Program of China (973 Program), which is Key Technology Research of Accelerator Driven Sub-critical System for Nuclear Waste Transmutation, and supported by the China Ministry of Science and Technology under Contract No. 2007CB209903.

[1] M. Avrigeanu, W. von Oertzen, U. Fischer, and V. Avrigeanu, Nucl. Phys. A **759**, 327 (2005).
[2] W. W. Daehnick, J. D. Childs, and Z. Vrcelj, Phys. Rev. C **21**, 2253 (1980).
[3] J. Bojowald, H. Machner, H. Nann, W. Oelert, M. Rogge, and P. Turek, Phys. Rev. C **38**, 1153 (1988).
[4] Y. L. Han, Y. Y. Shi, and Q. B. Shen, Phys. Rev. C **74**, 044615 (2006).
[5] S. Watanabe, Nucl. Phys. **8**, 484 (1958).
[6] F. G. Perey and G. R. Satchler, Nucl. Phys. A **97**, 515 (1967).
[7] M. Avrigeanu, H. Leeb, W. Von Oertzen, F. L. Roman, and V. Avrigeanu, in *Proceedings of the 11th International Conference on Nuclear Reaction Mechanisms, Varenna, 12–16 June 2006*, edited by E. Gadioli, p. 203.
[8] M. Avrigeanu, H. Leeb, W. von Oertzen, F. L. Roman, V. Avrigeanu, in *International Conference on Nuclear Data for Science and Technology, 22–27 April 2007* (EDP Sciences, 2007), p. 292.
[9] P. Schuck, Z. Phys. **241**, 395 (1971).
[10] Q. B. Shen, J. S. Zhang, Y. Tian, Z. Y. Ma, and Y. Z. Zhuo, Z. Phys. A **303**, 69 (1981).
[11] Q. B. Shen, Y. L. Han, and H. R. Guo, Phys. Rev. C **80**, 024604 (2009).
[12] J. S. Bell and E. J. Squires, Phys. Rev. Lett. **3**, 96 (1959).

[13] H. R. Guo, Y. Zhang, Y. L. Han, and Q. B. Shen, Phys. Rev. C **79**, 064601 (2009).
[14] J. W. Negele, Phys. Rev. C **1**, 1260 (1970).
[15] J. P. Jeukenne, A. Lejeune, and C. Mahaux, Phys. Rev. C **16**, 80 (1977).
[16] D. Vautherin and D. M. Brink, Phys. Rev. C **5**, 626 (1972).
[17] H. O. Meyer, P. Schwandt, W. W. Jacobs, and J. R. Hall, Phys. Rev. C **27**, 459 (1983).
[18] Q. B. Shen, D. C. Feng, and Y. Z. Zhuo, Phys. Rev. C **43**, 2773 (1991).
[19] A. Auce *et al.*, Phys. Rev. C **53**, 2919 (1996).
[20] S. Mayo, W. Schimmerling, and M. J. Sametband, Nucl. Phys. **62**, 393 (1965).
[21] G. P. Millburn, W. Birnbaum, W. E. Crandall, and L. Schecter, Phys. Rev. **95**, 1268 (1954).
[22] J. R. Wu, C. C. Chang, and H. D. Holmgren, Phys. Rev. C **19**, 370 (1979).
[23] I. Slaus and W. Parker Alford, Phys. Rev. **114**, 1054 (1959).
[24] P. R. Christensen, A. Berinde, I. Neamu, and N. Scintei, Nucl. Phys. A **129**, 337 (1969).
[25] K. Hatanaka, K. Imai, S. Kobayashi, T. Matsusue, M. Nakamura, K. Nisimura, T. Noro, H. Sakamoto, H. Shimizu, and J. Shirai, Nucl. Phys. A **340**, 93 (1980).
[26] G. Duhamel, L. Marcus, H. Langevin-Joliot, J. P. Didelez, P. Narboni, and C. Stephan, Nucl. Phys. A **174**, 485 (1971).
[27] O. Aspelund *et al.*, Nucl. Phys. A **253**, 263 (1975).
[28] C. C. Foster *et al.*, Bull. Am. Phys. Soc. **24**, 594 (1979); **24**, 838 (1979).
[29] A. Korff *et al.*, Phys. Rev. C **70**, 067601 (2004).
[30] W. Fitz, R. Jahr, and R. Santo, Nucl. Phys. A **101**, 449 (1967).
[31] G. Perrin *et al.*, Nucl. Phys. A **282**, 221 (1977).
[32] E. Newman, L. C. Becker, and B. M. Freedom, Nucl. Phys. A **100**, 225 (1967).
[33] F. Hinterberger *et al.*, Nucl. Phys. A **111**, 265 (1968).
[34] G. Duhamel *et al.*, Nucl. Phys. A **174**, 485 (1971).
[35] A. C. Betker, C. A. Gagliardi, D. R. Semon, R. E. Tribble, H. M. Xu, and A. F. Zaruba, Phys. Rev. C **48**, 2085 (1993).
[36] K. Hatanaka *et al.*, Nucl. Phys. A **340**, 93 (1980).
[37] A. Kiss *et al.*, Nucl. Phys. A **262**, 1 (1976).
[38] C. Baumer *et al.*, Phys. Rev. C **63**, 037601 (2001).
[39] L. D. Knutson and W. Haeberli, Phys. Rev. C **12**, 1469 (1975).
[40] J. M. Lohr and W. Haeberli, Nucl. Phys. A **232**, 381 (1974).
[41] R. P. Goddard and W. Haeberli, Nucl. Phys. A **316**, 116 (1979).
[42] R. D. Rathmell, P. J. Bjorkholm, and W. Haeberli, Nucl. Phys. A **206**, 459 (1973).
[43] H. R. Burgi *et al.*, Nucl. Phys. A **321**, 445 (1979).
[44] M. Ermer *et al.*, Nucl. Phys. A **533**, 71 (1991).
[45] R. Roche *et al.*, Nucl. Phys. A **220**, 381 (1974).
[46] A. Korff *et al.*, Phys. Rev. C **70**, 067601 (2004).
[47] R. K. Jolly, E. K. Lin, and B. L. Cohen, Phys. Rev. **130**, 2391 (1963).
[48] G. Perrin *et al.*, Nucl. Phys. A **206**, 623 (1973).
[49] T. Murayama *et al.*, Nucl. Phys. A **486**, 261 (1988).